
Article:
Li, G. orcid.org/0000-0002-5956-4033, Taras, P., Zhu, Z.Q. et al. (2 more authors) (2017) Investigation of Irreversible Demagnetization in Switched Flux Permanent Magnet Machines under Short-Circuit Conditions. IET Electric Power Applications, 11 (4). pp. 595-602. ISSN 1751-8660

https://doi.org/10.1049/iet-epa.2016.0189

Investigation of Irreversible Demagnetization in Switched Flux Permanent Magnet Machines under Short-Circuit Conditions

Guang-Jin Li [1*], Petrica Taras [1], Zi-Qiang Zhu [1], Javier Ojeda [2], and Mohamed Gabsi [2]

[1] Department of Electronic and Electrical Engineering, University of Sheffield, Sheffield, UK
[2] Systèmes et Applications des Technologies de l'Information et de l'Energie, Ecole Normale Supérieure de Cachan, Cachan, France
[*] g.li@sheffield.ac.uk

Abstract: The irreversible magnet demagnetization phenomena are investigated in this paper, under both healthy and short-circuit conditions for a switched flux permanent magnet (SFPM) machine. The temperature effects on permanent magnet material are taken into account and the influence of short-circuit current over demagnetization is evaluated. In order to calculate the short-circuit current (mainly inter-turn short-circuit), the MATLAB/Simulink model has been employed. The aforementioned short-circuit current is then fed to the finite element model, so the demagnetization analysis can be carried out. Various fault scenarios are investigated, including high speeds and high fault severity. It is found that the short-circuit current has limited effect on the magnet demagnetization due to particular features of the SFPM machines. The mechanism of demagnetization has been revealed and found out to be mainly due to temperature rise and poor PM materials utilization. Experiments have been carried out to validate the MATLAB/Simulink model for short-circuit current predictions.

1. Introduction

PERMANENT magnet (PM) brushless machines are becoming increasingly attractive for the aircraft and automotive industries due to several important advantages such as high torque density, wide speed range, excellent robustness and fault-tolerant capability. These characteristics are desirable for aircraft applications where there is a trend to replace traditional mechanical actuators with the more efficient and reliable electrical ones [1].

The switched flux permanent magnet machines (SFPMMs) [2], [3], as shown in **Fig. 1** (a), meet most, if not all, of the aforementioned requirements, while standing out in comparison with other PM machines. A SFPMM has a doubly salient structure, consisting of a passive rotor similar to that of a switched reluctance machine, making it suitable for high speed applications. Moreover, the stator houses both the PMs and the concentrated non-overlapping windings, providing easy access to cooling for both the windings and PMs. The PMs are circumferentially and alternatively magnetized and sandwiched by U-shape iron segments, which are wounded by the concentrated non-overlapping armature coils. The SFPMMs have been extensively studied in the past decade, being known to have bipolar flux-linkage and sinusoidal back-EMF, which makes them suitable for brushless alternating current (BLAC) drive and can achieve high torque density and wide constant power speed range. When compared with other PM machines, especially with rotor mounted ones, it was shown that SFPMM exhibits the same if not better

performance [4], [5], [6], [7], [8]. The SFPMM also showed superior performance over other stator mounted PM counterparts [8], [9], [10], [11] such as the doubly salient and flux reversal PM machines. The doubly salient PM machines exhibit unipolar flux linkage due to PM locations in the stator yoke, leading to smaller torque density when compared with the SFPMM. The flux reversal PM machines, although they can have bipolar flux linkages, has its PM adjacent to the airgap, being subjected to demagnetization risks and radial forces.

The original conventional SFPM machine with double layer windings lacks the fault-tolerant capability since there are no electromagnetic and thermal separations between two adjacent coils or phases. However, this can be addressed by changing the double layer winding layout to a single layer type [12] or by adopting the E-core topology [13], [14], [15] which also uses less PM material.

However, despite the enumerated advantages, the key weakness of SFPMMs and other PM machines are the PMs which are prone to demagnetization [16], [17], [18]. This is possible, especially in the aircraft applications where the machine might be subjected to a large range of operating temperatures (-50^{o}C to 150^{o}C) which can irreversibly affect the PMs' magnetic properties. This is particularly the case for SFPMM because its PMs are inside the armature coils, being close to the heat source, particularly in the case of a short-circuit fault.

Despite the fact that demagnetization is a serious issue, it has not been intensively investigated for SFPMMs when compared with other PM machines. The overall conclusion, based on the few existing papers on this subject, is that the machine is resilient to demagnetization under most operating scenarios, provided that the PM temperature is kept low [19], [20], [21], [22]. In [19], based on the machine's magnetic flux path, a demagnetization investigation under healthy operation is conducted for a rare earth SFPMM. It is demonstrated that regardless of the signs of *d*- and *q*-axis currents, the armature MMF is always parallel to the PM produced flux and hence will not demagnetize the magnets. In [20], a demagnetization analysis of SFPMM with ferrite magnets is conducted under both motor and generator modes. It is found out that partial demagnetization occurs mainly due to machine topology (due to the end effect of the PM being exposed to the airgap), which also affects the machine performance such as output torque. Finally, in [21] a study considering higher operating temperature is conducted, showing the possibility of irreversible demagnetization.

It should be noted that the previous investigations were made mainly under healthy conditions. The demagnetization phenomena has rarely, if ever, been investigated under faulty conditions and especially during a (phase or inter-turn) short-circuit. Therefore, the potential irreversible PM demagnetization in a 3-phase double layer conventional SFPMM is investigated under short-circuit conditions. The types of faults considered are inter-turn short-circuits affecting partially one phase, which are difficult to identify and can be destructive for winding insulations. The temperature dependent properties of PM material are

considered over a range of 25°C to 150°C which covers most of the operating temperatures in the automotive and aircraft applications.

2. The Investigated Machine and Considered Fault

By way of example, a 3-phase conventional double layer SFPMM is used for investigation. It has a 12-slot/10-pole and 4 series connected coils per phase, Fig. 1 (a). The machine main parameters are given in Table 1. The inter-turn short-circuit fault was chosen as it is the most common fault in electrical machines, and potentially could be more severe than a terminal short-circuit fault of an entire phase [23]. It occurs in one coil of phase A, which is named the faulty component of the phase A. Accordingly, the remaining three coils of the phase A will be referred to as the healthy components.

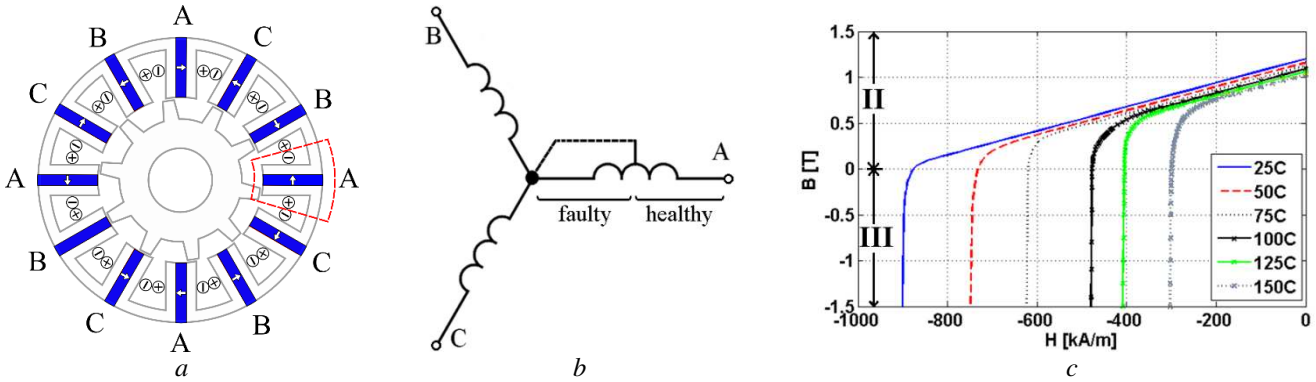

a *b* *c*

***Fig. 1**. The investigated SFPMM topology with short-circuit in one coil of the phase A.*
a Cross-section of SFPM
b Simplified circuit diagram of three phases
c B(H) curves of NdFeB magnets used for different temperatures

Table 1 Specification of the investigated machines

Stator slot number	12	Stator yoke height (mm)	3.6
Rated speed (rpm)	400	Stack length (mm)	25
Rated current (A)	11	Air-gap length (mm)	0.5
Rated torque (Nm)	2.2	Rotor outer radius (mm)	27.5
Stator outer radius (mm)	45	Magnet thickness (mm)	3.6
Stator inner radius (mm)	28	Number of turns/phase	72

Since the fault severity is also studied, a parameter α is introduced, which is defined as the ratio of short-circuited turns over the total number of turns in the affected phase and can vary between 1.4 % (one turn short-circuited) and 100 % (the whole phase short-circuited). This will be used in the following sections for faulty modelling based on MATLAB/Simulink to predict the short-circuit currents during different faulty conditions, which will then be used for magnet demagnetization analyses.

The PM material used in this paper is the high energy rare earth Neodymium Iron Boron (NdFeB) N35H compound [24] which is typical for SFPMMs. Ferrite magnets are not considered here because their demagnetization withstand capability improves with temperature rise. In order to accurately consider the demagnetization phenomena, a special consideration is given to the PM material model. The FE model keeps tracking and updating the magnet remanence (B_r) in each mesh element if the demagnetizing magnetic field strength drops locally below the knee point. This allows the PM material to recoil on a minor loop and to account for post-demagnetization performance. To consider the temperature influence on the demagnetization process, the demagnetization curves i.e. B(H), as shown in **Fig. 1** (c), are used [25]. This is important as the knee points vary with temperatures, moving from the third quadrant at low temperatures into the second quadrant at higher temperatures [26], [27]. For each curve in **Fig. 1** (c) the knee point and the magnet remanence are summarized in Table 2 for comparison.

Table 2 Characteristics of PM material

Temperature [°C]	25	50	75	100	125	150
B_r [T]	1.20	1.16	1.13	1.09	1.06	1.03
B_{knee} [T]	-0.08	0.03	0.20	0.28	0.40	0.50

3. Fault Modelling of SFPMMs

3.1. Method of Investigation

The investigation method makes full use of a combination of FE and MATLAB/Simulink models. The FE package used is Flux software from Cedrat. Firstly, FE models are used to retrieve parameters like inductances, back-EMF and cogging torque which will then be used to establish the Simulink models. Then, the Simulink models will generate the armature currents for different short-circuit conditions. Finally, these currents (healthy and short-circuit) are used in the magneto-static FE models to assess the aforementioned demagnetization.

The cogging torque and back-EMF are both temperature and rotor position dependent. In particular, the back-EMF is calculated for both faulty and healthy components of the phase A. For each case, the affected PM properties are adjusted so to account for different temperatures in Table 2, while the remaining (unaffected) PMs are assumed to work at the normal condition of 25°C. The inductances were considered to be independent of temperature, depending only on their rotor position. At the extreme temperature values (25 and 150^{o}C) the inductance difference is less than 10%. In addition, further

investigation has shown that the influence of phase armature current on average self and mutual inductances is negligible for the given phase current range.

A post-fault control strategy (speed control) is required and hence Simulink models are used in the investigation. The output of the Simulink models mainly concerns the short-circuit and healthy currents. Four typical rotor positions of interest are selected (the positive and negative *d*- and *q*-axes) and used in the static FE models. By investigating the component parallel to the magnetization direction of the flux density (B_m) of the affected PM and comparing it with the knee point values from Table 2 for each temperature, one can predict the nature of the magnet demagnetization (reversible or irreversible).

It is worth noting that the use of alternative solutions to the method presented above is possible. For example, the co-simulation solution, which implies the coupling of Simulink with the FEM software. However, this method is very time consuming due to a small simulation time step which needs to be accurate enough to deal with all the higher order harmonics generated by the PWM block.

3.2. Dynamic Faulty Model

A simple but accurate dynamic faulty model is implemented starting from equation (1), which is typical [12], [28], [29] for all synchronous machines.

$$[v] = [R] \cdot [i] + \frac{d([L] \cdot [i])}{dt} + [e] \tag{1}$$

where $[v]$, $[i]$ and $[e]$ are the phase voltage, phase current and back-EMF vectors, being described by the following expressions:

$$[v] = \begin{bmatrix} v_h \\ v_b \\ v_c \\ v_f \end{bmatrix}, [i] = \begin{bmatrix} i_h \\ i_b \\ i_c \\ i_f \end{bmatrix}, [e_0] = \begin{bmatrix} e_h \\ e_b \\ e_c \\ e_f \end{bmatrix} \tag{2}$$

The indexes *b* and *c* denotes the phases *B* and *C* related quantities while *h* and *f* indicates the healthy and faulty components of the affected phase *A*. During normal operation, $i_h = i_f$ (short-circuit current) and $v_a = v_f + v_h = \alpha v_a + (1-\alpha) v_a$, i.e. the faulty and healthy components of phase *A* are series connected. During short-circuit, $v_a = v_h$, $v_f = 0$ and $i_h \neq i_f$ which means that the short-circuited coil is separated from the rest of phase *A* and it is no longer controllable. In case that v_f is not zero (i.e. a contact resistance exists at the short-circuit point), the short-circuit current will be reduced. $[R]$ and $[L]$ are the resistance and inductance matrices, characterizing the phases with special attention paid to the faulty and healthy components of phase *A*. The resistance matrix $[R]$ is given by:

$$[R] = \begin{bmatrix} R_h & 0 & 0 & 0 \\ 0 & R & 0 & 0 \\ 0 & 0 & R & 0 \\ 0 & 0 & 0 & R_f \end{bmatrix} \tag{3}$$

where R is the phase resistance which is temperature dependent as the copper resistivity increases with temperature. The $R_h = (1-\alpha)R$ and $R_f = \alpha R$ are the resistance values of the healthy and faulty components of phase A. The inductance matrix $[L]$ is given by (4):

$$[L(\theta)] = \begin{bmatrix} L_h & M_{Bh} & M_{Ch} & M_{fh} \\ M_{hB} & L_B & M_{CB} & M_{fB} \\ M_{hC} & M_{BC} & L_C & M_{fC} \\ M_{hf} & M_{Bf} & M_{Cf} & L_f \end{bmatrix} \tag{4}$$

where the h and f subscripts are referring again to phase A only. $[L]$ contains both self and mutual inductances as functions of rotor positions, which are determined using FE models and can be depicted in Fig. 2.

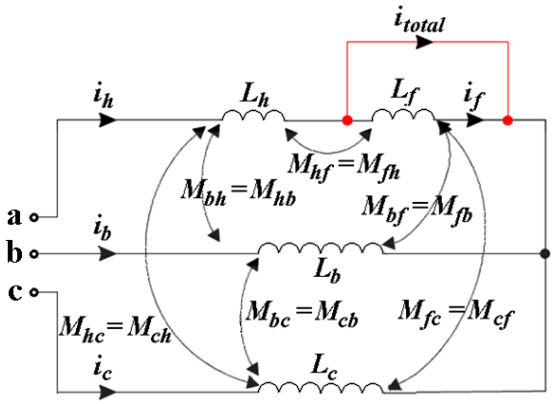

Fig. 2. *Self and mutual inductances between various phases when inter-turn short-circuit fault within one phase occurs [28]. i_h is the healthy current, i_f is the short-circuit current and i_{total} is the resultant current of the phase A.*

The typical mechanical model is described by

$$T_{em} + T_{cogg} + T_{reluct} = J \cdot \frac{d\Omega}{dt} + f \cdot \Omega + T_{load} \tag{5}$$

where T_{em}, T_{cogg}, T_{reluct} and T_{load} are the magnet excitation, cogging, reluctance and load torques, respectively. J is the moment of inertia, f is the friction coefficient, Ω is the rotor mechanical speed and p = 10 is the rotor pole number, respectively. T_{em} is given by $p[\phi]^t[i]$ where $[\phi]$ is the open circuit flux linkage and it is associated with the back-EMF vector $[e]$. $[i]$ represents the phase currents. The cogging torque has been extracted from FE models as temperature and rotor position dependent. The average value of reluctance torque is negligible under healthy conditions and balanced operation but cannot be neglected during short-circuit operations [30]:

$$T_{reluct} = \frac{1}{2} \cdot \sum_{k}^{h,f,b,c} \frac{dL_k}{d\theta} \cdot i_k^2 + \sum_{k,j;k\neq j}^{h,f,b,c} \frac{dM_{k,j}}{d\theta} \cdot i_k \cdot i_j \quad (6)$$

3.3. Simulink Model and Associated Results

The Simulink model implements the equations from (1) to (6). The MTPA (maximum torque per ampere) control strategy is used during both the healthy and faulty operations, **Fig. 3** (a). Since there is no reluctance torque [3] during normal operation, this strategy implies I_d = 0 A current control. Two controllers have been used, e.g. a PI speed controller (K_p=3.33, K_i=2) and a PI current controller (K_p=10, K_i=50), in order to maintain the same average torque and speed after the aforementioned fault occurs.

Using this model, the peak short-circuit current as a function of speed is obtained, as shown in Fig. 3 (b), which is also for various temperatures. It can be seen that the highest short-circuit current is achieved when the temperature is the lowest. In addition, the short-circuit currents do not change significantly for low temperature cases such as from 25°C to 75°C. The back-EMF induced in the short-circuited coil as well as the phase resistance are influencing the short-circuit current and are temperature dependent. The back-EMF decreases while the resistance increases with temperature, thus limiting the short-circuit current at high temperatures. However, at higher temperature there is an additional phenomena which also contributes to reduce the short-circuit current, as will be detailed in section 5.

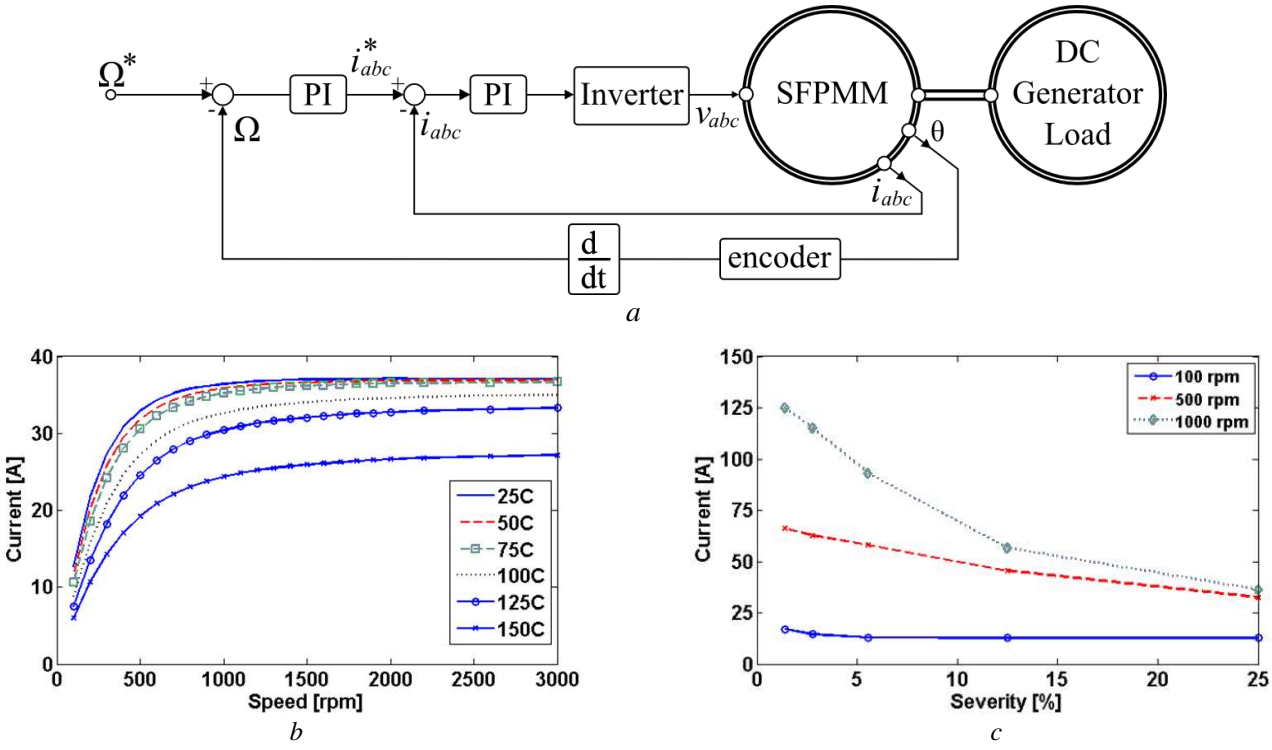

Fig. 3. *Control schematic of the machine and peak short-circuit currents for various scenarios*
a Control diagram
b Peak short-circuit current vs speed and temperature (25% fault severity – 1 out of 4 coils short-circuited),
c Peak short-circuit current vs fault severity at 25°C.

The influence of fault severity on short-circuit current is also investigated, using the same Simulink model, as shown in **Fig. 3** (c). The short-circuit fault severity varies from 1.4% to 25%, corresponding to a short-circuit of 1 to 18 out of 72 turns per phase. The entire fault severity study concerns only one coil out of four, for three different speeds. Beyond 1000 rpm, the short-circuit current can be regarded as independent of rotor speed as shown in **Fig. 3** (b). Furthermore, the study is conducted at a low temperature (25°C) in order to obtain the highest short-circuit currents.

It is found in **Fig. 3** (c) that for different speeds, the one turn short-circuit is the worst scenario as the current will reach a significantly high value, e.g. 125A for 1000 rpm, which is around 10 times the rated current (11A). The short-circuit current variation with fault severity can be explained using (7) which gives the approximate short-circuit current peak value (by neglecting mutual coupling with the other phases as well as the contact resistance at the short-circuit point):

$$i_{sc} \approx \frac{\alpha \cdot E_{max}}{\sqrt{(\alpha \cdot R)^2 + (\alpha^2 \cdot \omega \cdot L)^2}} \approx \frac{\omega \cdot \Phi_{max}}{\sqrt{R^2 + (\alpha \cdot \omega \cdot L)^2}} \tag{7}$$

where R and L are the phase resistance and self inductance, E_{max} and Φ_{max} are the peak values of the back-EMF and phase flux linkage while ω is the angular electric speed. Since the winding is concentrated, the flux due to PMs through the affected coil will be constant for all fault severities. The only term in (7) varying with the fault severity α parameter is $\alpha^2\omega L$ (reactance), which is negligible compared to R^2 at low speed while becoming important at high speed. Therefore, at low speed the current does not vary significantly with the fault severity as it is mainly determined by the constant ratio $\omega\Phi_{max}/R$. However, at high speed both the back-EMF and the reactance term are increasing, cancelling the influence of R. The contribution of α is much more pronounced now as it will reduce the reactance term, thus increasing the short-circuit current, as shown in **Fig. 3** (c).

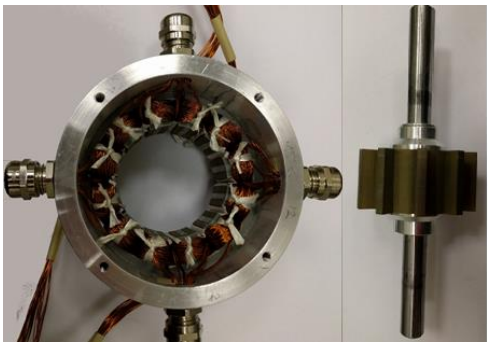

a

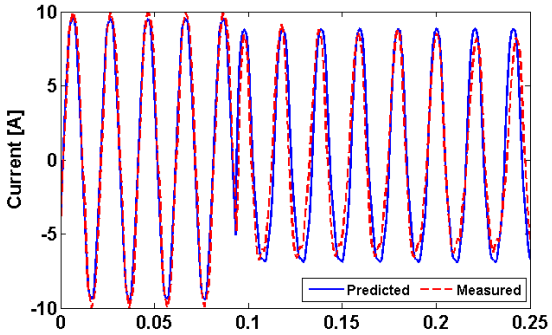

b

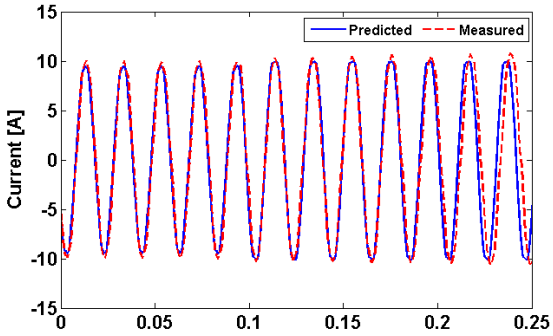

c

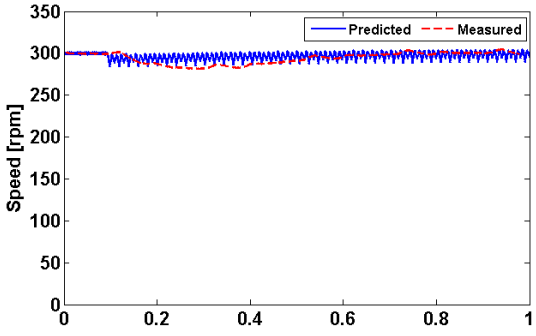

d

Fig. 4. *Prototype and comparison between measured and predicted results (25% fault severity – 1 out of 4 coils short-circuited).*
a Prototype machine: stator and rotor.
b i_f short-circuit current.
c i_b phase current
d Speed.

In order to validate the FE and Simulink models a SFPMM prototype, **Fig. 4** (a), is built and tested according to methodologies used in [12], [28]. The dSPACE framework was used to implement the control strategies. The comparison between predicted and measured results is given in **Fig. 4**. The experimental validation is carried out for low temperature and moderate speed (25 °C & 300 rpm). A load torque of 1.44 Nm is introduced. Also, a low fault severity of 25% is considered to prevent damaging the machine during tests. The short-circuit is introduced at around 0.1 s. It can be observed that the predicted currents match well with the measured ones, as shown in Fig. 4 (b)-(c), so do the speeds, as shown in Fig. 4 (d). This validates the adopted FE and Simulink models.

4. Demagnetization Investigation under Short-Circuit Conditions

4.1. Low Speed Short-Circuit

At first, using the aforementioned faulty model, the short-circuit operation is investigated at low fault severity (25% turns short-circuited) and low speed (100 rpm), so the short-circuit current is kept low. This can establish a baseline to analyse temperature dependent demagnetization because the influence of short-circuit current could be negligible.

Fig. 5 shows the demagnetized areas in the affected PM [the coil around this PM is short-circuited, as shown in Fig. 1 (a)] for two selected temperatures (25°C and 150°C). Only the positive *d*-axis (27° mech.) and negative *q*-axis (0° mech.) positions are shown. At low temperatures, as shown in Fig. 5 (a) and (b), the demagnetization occurs only locally, due to end effects. However, at 150°C, as shown in Fig. 5 (c) and (d) the entire PM area is demagnetized regardless of rotor position.

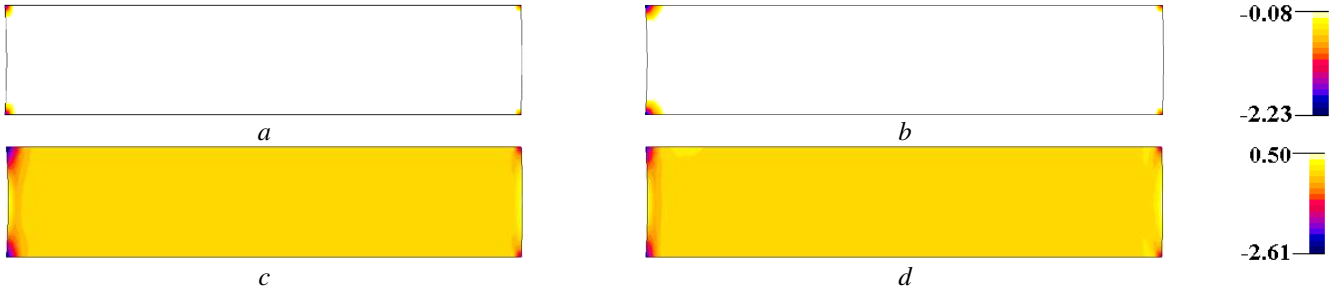

Fig. 5. *Demagnetization flux density colour maps (white – not demagnetized, coloured – demagnetized) with 25% short-circuit at 100 rpm. Left-hand side is adjacent to the airgap.*
a Positive d-axis 25° C
b Negative q-axis 25° C
c Positive d-axis 150° C
d Negative q-axis 150° C.

In order to better compare various temperature cases, the nodal flux densities (circumferential components) along the central line of the affected PM are shown in **Fig. 6** (d). For completeness, the results of a healthy case are also included. The cross-coupling effect between armature current and PM lowers the working point of the PMs for the healthy and short-circuit cases. However, the demagnetization due to the cross-coupling is weak and therefore is not detailed here.

The working point for all temperature cases in Fig. 6 are already much lower than the relevant remanence (B_r) from Table 2, even for the healthy case. This is mainly due to the influence of the magnetic circuit. However, the influence of temperature is much more significant, which lowers the working point even further. The lowest working point (<0.4 T) for all cases, is achieved in q-axis, as shown in **Fig. 6** (b). For high temperature cases, e.g. 150°C, the local flux density) in the affected PM can have reversed polarity with respect to the PM magnetization direction, as shown in **Fig. 6**, and hence be heavily demagnetized. This will be investigated in more depth in section 5.

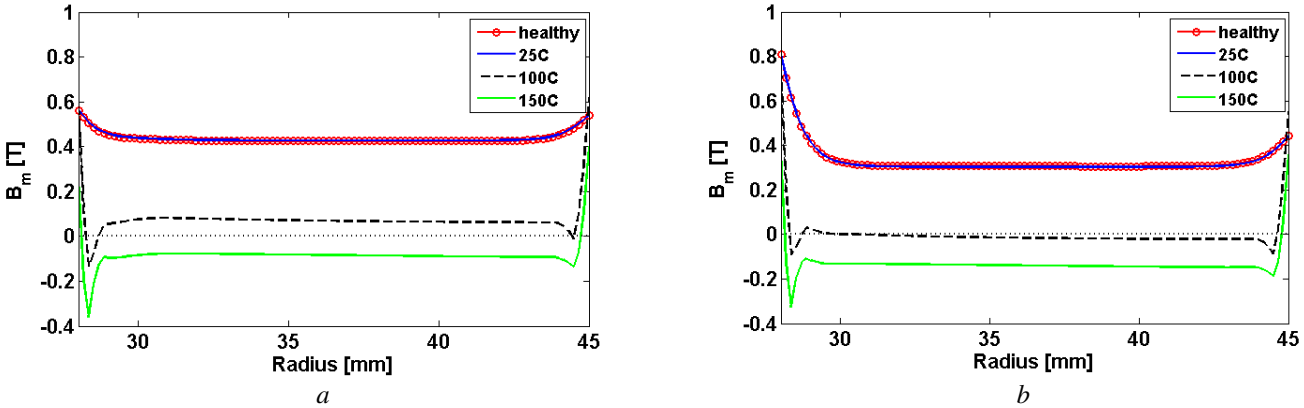

a *b*

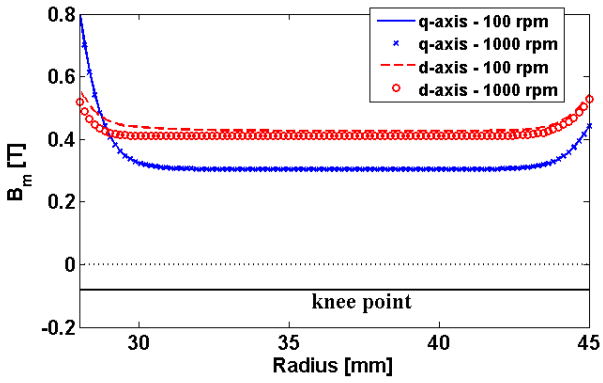

c

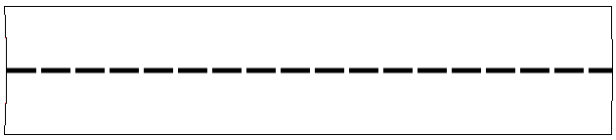

d

Fig. 6. *Flux densities (circumferential components) along the central line affected PM*
a Positive d-axis (27° mech.), (25% short-circuit at 100 rpm)
b Negative q-axis (0° mech.), (25% short-circuit at 100 rpm)
c Positive d-axis (27° mech.) and negative q-axis (0° mech.), (25°C & 25% fault severity)
d The path (dashed line) through the middle of the PM on which the B_m is represented.

The irreversible demagnetization phenomena occur when the operating temperatures are high enough, e.g. ≥100°C. Under all aforementioned conditions, the peak short-circuit current is lower than the rated current due to low speed used, as shown in Fig. 3 (b). Therefore, the demagnetization of the affected PM could only be due to the influence of the adjacent PMs and temperature rise. However, it is possible that higher speeds can result in higher demagnetizing short-circuit currents, which would aggravate the magnet irreversible demagnetization. This will be investigated in the following section.

A summary of irreversible demagnetization of the studied cases at low speed is given in Table 3.

Table 3 Demagnetization Summary: 25% Short-Circuit at 100 rpm

Temperature [°C]	25	50	75	100	125	150
	no	**no**	**no**	**yes**	**yes**	**yes**

'**yes**' or '**no**' means irreversible demagnetization in a large area of magnet has occurred or not

4.2 High Speed Short-Circuit

The 25°C, 100rpm or 1000rpm with 25% short-circuit case is used in order to assess the magnet irreversible demagnetization, as shown in **Fig. 6** (c). The low temperature is chosen as the short-circuit current could be maximum, based on results shown in Fig. 3 (b). This can also eliminate the influence of temperature on magnet demagnetization so that the investigation in this section can be focused on the influence of the short-circuit current. For the selected speed (1000rpm), the resulting current is within 95% of the maximum achievable short-circuit current (for this fault severity). It is found that in the *q*-axis the armature winding flux does not influence the working point of the PMs, as shown in **Fig. 6** (c). However, regarding the positive *d*-axis the increase in the short-circuit current (from 6.3 to 36 A) has only a slight

demagnetizing effect. Similar results were obtained for higher fault severities and therefore are not presented to avoid duplication. One can then draw a conclusion that the SFPMM is robust against magnet demagnetization at low temperature, even under short-circuit conditions.

5. Discussion on Demagnetization Mechanism

In order to analyse the previously observed magnet demagnetization due to short-circuit and temperature, the influences of the armature MMF and PM field on demagnetization are separated using the well-established frozen permeability (FP) method [31], which has been validated before using in this paper. Since the FP method based on the finite element model is only a tool for analysis, its principle will not be repeated. The short-circuits investigated in this section concerns two cases, i.e. low temperature (25°C) and high temperature (150°C), both are at high speed (1000 rpm) and 25% fault severity. This will give an insight into the demagnetization process evolving from lower to higher temperature. Other temperatures achieve similar results. Therefore, they are not shown here. Fig. 7 shows the nodal circumferential flux densities (B_m) along the central line of the affected PM obtained from two static FE models. The first FE model contains the influence of both PM and current sources. However, in the second FE model, the PMs are the only sources of magnetic field, while saturation level of the magnetic circuit is kept unchanged using the FP method. Two rotor positions (positive *d*- and negative *q*-axes) are considered for each temperature.

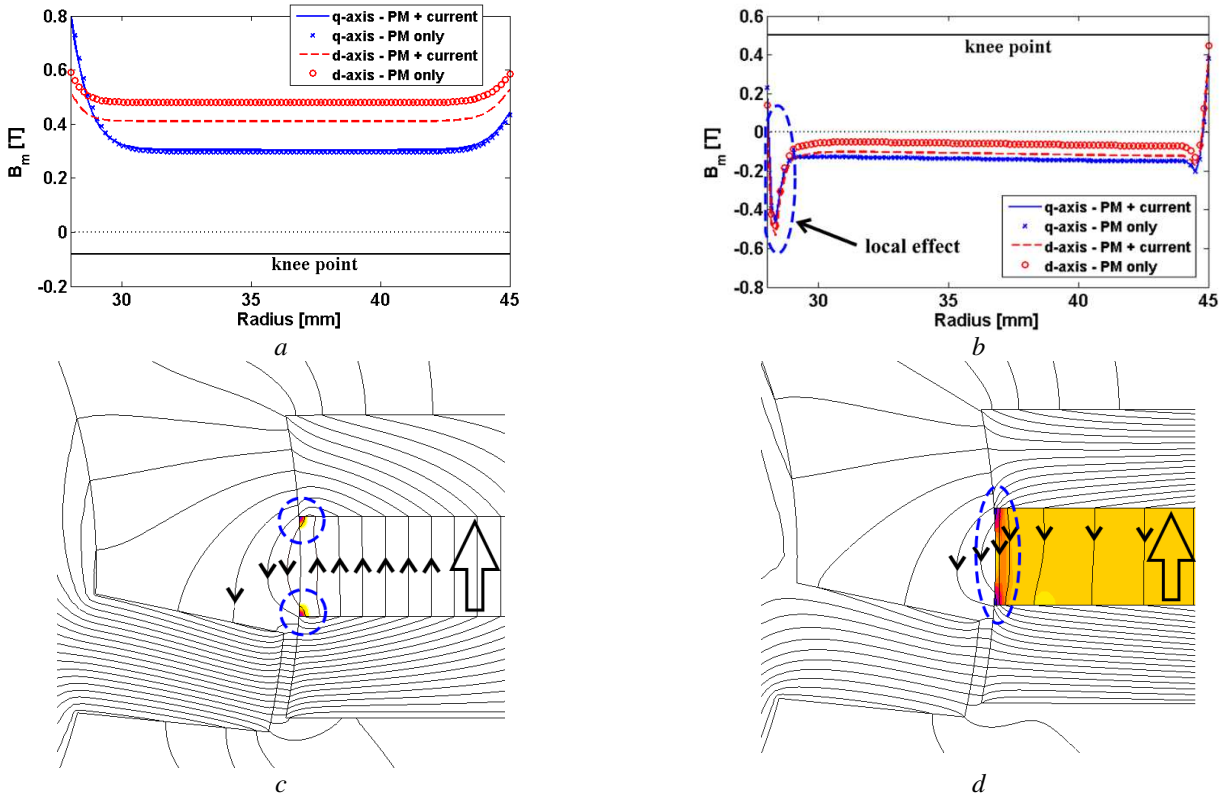

Fig. 7. *The circumferential flux density component through affected PM at 1000rpm & 25% fault severity and local*

phenomena detailing.
a Negative q-axis (0° mech.) and positive d-axis (27° mech.) at 25°C
b Negative q-axis (0° mech.) and positive d-axis (27° mech.) at 150°C
c Positive d-axis (27° mech.) at 25°C local demagnetization phenomena detailing
d Positive d-axis (27° mech.) at 150°C local demagnetization phenomena detailing.

Based on Fig. 7 it can be seen that adding the current sources only contributes to a reduction of the magnet working point in the *d*-axis. This is the case for all studied temperatures. The reduction is due to the short-circuit current, which is equivalent to a demagnetizing *d*-axis current. However, for all temperatures, the PM flux densities in *q*-axis are lower than that in *d*-axis, resulting in more severe demagnetization. It is also found that at low temperature, as shown in Fig. 7 (a), the PM flux densities are higher than its knee point, and hence has not been irreversibly demagnetized. Moreover, the PM flux densities along the central line of the affected PM first reduce and increase thereafter with the increasing radius (from 28.5mm to 45mm). This is the case for both *d*- and *q*-axes. However, for high temperature as shown in Fig. 7 (b), the PM flux densities are lower than its knee point, resulting in severe irreversible demagnetization in both axes. Moreover, there are some local effects at both ends of the affected PM due to magnetic circuit configuration which can enhance local flux lines or reduce them, depending on the PM working temperature. This is explained further in Fig. 7 (c) and (d) which shows both the local flux lines as well as the PM demagnetized areas (colour map). The natural PM magnetization is represented with a big hollow arrow while the direction of the local flux lines is given by small arrows superimposed over them. At low temperature the demagnetization has occurred only at the corners of the affected PM adjacent to the airgap, a local effect which was noticed in [20] as well. However at 150°C, general demagnetization occurs in the affected PM with a much worse local phenomena close to the PM edge, Fig. 7 (d). Upon closer inspection, this high temperature local effect is the outcome of the evolution of the initial demagnetized areas from low temperature (before short-circuit). These initial areas are expanded at each time steps (FE model) until they merge forming a bridge, as shown in Fig. 7 (d), between the PM corners from Fig. 7 (c). This is due to a stronger local reduction of the B_r at each time step when compared to the rest of the PM. Therefore at high temperature the enhanced local demagnetization effect at the PM edge is facilitating more the crossing of demagnetizing flux than in the rest of the affected PM. The consideration of this effect is possible only due to the fact that the FE model can update the PM remanent flux density at each time step – this phenomena will not be noticeable with classic linear PM models.

In order to explain the previously observed phenomena in Fig. 7 (a) and (b), the following analysis has been carried out. Since the demagnetization contributions of both PMs and armature currents can be separated accurately using the FP method, their influence on magnet demagnetization can be analysed separately. Fig. 8 allows a comparison between the PM fluxes at low and high temperatures. At low temperature, the PM is unaffected even though it is under the influence of high short-circuit current. At

high temperature, the flux paths change significantly, in particular the flux (Φ_{PM}) generated by the affected PM can be reduced or even eliminated. This can be explained using superimposed, simplified flux paths over the existing flux lines, which helps to identify and compare the influence of adjacent PMs on the affected one.

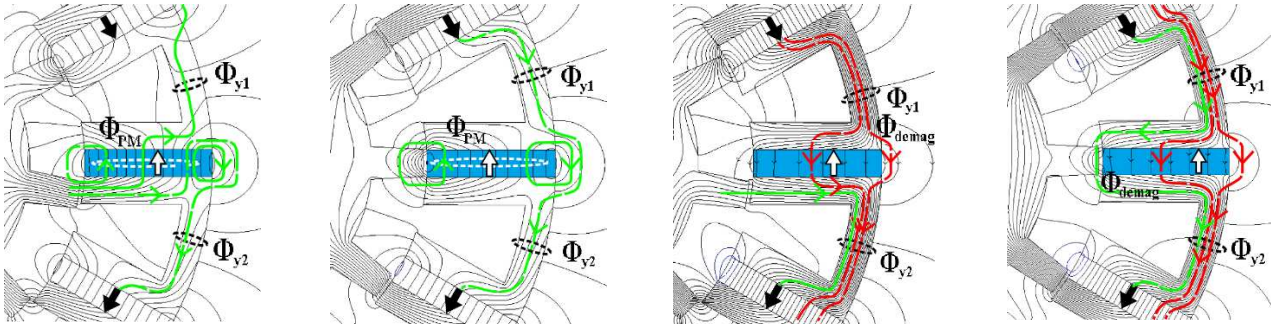

a *b* *c* *d*

Fig. 8. *Flux line distributions due to PM only at 1000rpm & 25% fault severity, which is separated from flux due to armature current using FP method and their associated simplified flux diagrams.*
a Positive d-axis (27° mech) 25° C
b Negative q-axis (0° mech.) 25° C
c Positive d-axis (27° mech) 150° C
d Negative q-axis (0° mech.) 150° C.

The flux line distributions at low temperature (25°C), are shown in **Fig. 8** (a) and (b). Three flux components can be identified in the area surrounding the affected PM. These are the yoke fluxes Φ_{y1}, Φ_{y2} and the PM flux Φ_{PM} generated by the affected PM. For low temperature, it can be seen that the yoke fluxes (Φ_{y1} and Φ_{y2}) are equal regardless of the rotor position. When it comes to high temperature (150°C), as shown in **Fig. 8** (c) and (d), there can be an extra flux component, the demagnetization flux Φ_{demag}, crossing the affected PM in an opposite direction to its magnetization.

The demagnetizing component Φ_{demag} depends strongly on the yoke fluxes generated by the two adjacent PMs. By way of example, based on **Fig. 8** (c), it can be seen that for the *d*-axis the yoke fluxes are not equal with one of them being higher than the other ($\Phi_{y1} < \Phi_{y2}$). Some of the yoke fluxes are diverted from the affected PM due to rotor tooth alignment with the stator tooth, which lowers or cancels the Φ_{demag} component. As a result, the irreversible demagnetization at *d*-axis is not so severe, as shown in Fig. 6 and Fig. 7. However, when it comes to the *q*-axis in **Fig. 8** (d), the yoke fluxes are equal and contributing in the same manner to Φ_{demag}. Therefore, for this rotor position, the influence of adjacent PMs on the affected one is the same. The demagnetizing flux flows from the upper adjacent PM, crosses the affected PM and enters into the lower adjacent PM without being diverted into other parts of the machine and results in the highest demagnetization.

Despite that the simplified flux lines in **Fig. 8** are for the 25°C and 150°C cases, the analysis can be extended to other temperatures. For example, for short-circuit at 75°C, the demagnetization phenomena will not occur as the knee point is low enough. Therefore, the Φ_{demag} component does not exist similar to

the case at 25°C. Also, this type of analysis can be extended to analyse the influence of current sources on magnet demagnetization. In this case, only the *d*-axes need to be investigated with the armature flux enhancing (positive *d*-axis) or decreasing (negative *d*-axis) Φ_{demag}.

It is worth highlighting that in section 3 it was found that the short-circuit current decreases as the temperature increases, as shown in Fig. 3 (b). This is due to the phase back-EMF and resistance combined effect. However, for temperatures ≥ 100°C the short-circuit current decreases at a much faster pace. At lower temperatures (≤75°C), the back-EMF drop (hence short-circuit reduction) is due to reduction in the remanent flux density only. When it comes to higher temperatures, the irreversible demagnetization occurs in a significant (or even entire) volume of the affected PM. This would lead to a further decrease in the remanent flux density. As a results, since the PM working point is located on a lower recoil line, the resulting back-EMF in the short-circuit coil drops even further.

6. Conclusions

This paper has used the MATLAB/Simulink based faulty model and the frozen permeability (FP) method to investigate the influence of inter-turn short-circuit on magnet irreversible demagnetization of a conventional SFPMM. The influence of other factors such as rotor speed, and PM operating temperatures has also been taken into account. It was found that the SFPMM is extremely resilient to magnet demagnetization in *d*-axis and at low temperature although the short-circuit current is the highest in this condition. The main factor which contributes to the SFPMM robustness against demagnetization is the magnetic circuit configuration. The affected PM is shielded by two U-shaped iron segments which divert the demagnetizing fluxes from the affected PM, and preventing it from being demagnetized. Therefore, the short-circuit current and adjacent PMs have slight influence on the affected PM. At higher temperature, the short-circuit current is lower due to increased phase resistance, reduced magnet remanence and hence reduced phase back-EMF. However, the knee point is higher and the PM material has much lower coercivity which enables the adjacent PMs to easily demagnetize the affected one. Due to magnetic circuit alignment the highest irreversible demagnetization occurs in the *q*-axis, which can simplify the post-demagnetization analysis as only these particular positions need to be investigated.

7. References

[1] Sarlioglu B., Morris, C. T.: 'More electric aircraft: review, challenges, and opportunities for commercial transport aircraft', IEEE Trans. Transport. Electrific., **1**, (1), June 2015, pp. 54 - 64.

[2] Rauch, S. E., Johnson, L. J.: 'Design principles of flux-switch alternators', Power apparatus and systems, part III, Transactions of the American Institute for Electrical Engineers, **74**, (3), January 1955.

[3] Zhu, Z. Q., Pang, Y., Howe, D., *et al.*: 'Analysis of electromagnetic performance of flux-switching permanent-magnet machines by nonlinear adaptive lumped parameter magnetic circuit model', IEEE Trans. Magn., **41**, (11), November 2005, pp. 4277-4287.

[4] Pang, Y., Zhu, Z. Q., Howe, D., *et al.*: 'Comparative study of flux-switching and interior permanent magnet machines', Proc. ICEMS, Seoul, South Korea, 8-11 October, 2007.

[5] Cao, R., Mi, Cheng, M.: 'Quantitative comparison of flux-switching permanent-magnet motors with interior permanent magnet motor for EV, HEV, and PHEV applications', IEEE Trans. Magn., **48**, (8), August 2012, pp. 2374 - 2384.

[6] Fasolo, A., Alberti, L., Bianchi, N.: 'Performance comparison between switching-flux and IPM machines with rare-earth and ferrite PMs', IEEE Trans. Ind. Appl.,**50**, (6), December 2014, pp. 3708 - 3716.

[7] Thomas, A. S., Zhu, Z. Q., Jewell, G. W.: 'Comparison of flux switching and surface mounted permanent magnet generators for aerospace applications', Proc. PEMD 2010, Brighton, UK, 19-21 April 2010

[8] Hua, W., Cheng, M., Zhu, Z. Q., *et al.*: 'Comparison of electromagnetic performance of brushless motors having magnets in stator and rotor', Journal of Appl. Phys., **103**, 12 March 2008.

[9] Cheng, M., Hua, W., Zhang, J., *et al.*: 'Overview of stator-permanent magnet brushless machines', IEEE Trans. Ind. Electron., **58**, (11), November 2011, pp. 5087-5101.

[10] Hua, W., Cheng, M., Hongyun, J., *et al.*: 'Comparative study of flux-switching and doubly-salient PM machines particularly on torque capability', in IEEE Ind. Appl. Society Annu. Meeting, Edmonton, Canada, 5-9 October 2008.

[11] Zhang, J., Cheng, M., Chen, Z.: 'Investigation of a new stator interior permanent magnet machine', IET Elect. Power Appl., **2**, (2), March 2008, pp. 77-87.

[12] Li, G. J., Ojeda, J., Hoang, E., *et al.*: 'Double and single layers flux-switching permanent magnet motors: Fault tolerant model for critical applications', Proc. ICEMS, Beijing, 20-23 August 2011.

[13] Zhu, Z. Q., Chen, J. T.: 'Advanced flux-switching permanent magnet brushless machines', IEEE Trans. Magn., **46**, (6), June 2010, pp. 1447 - 1453.

[14] Chen, J. T., Zhu, Z. Q., Iwasaki, S. *et al.*: 'A novel E-core flux-switching PM brushless AC machine', Proc. ECCE 2010, Atlanta, USA, 12-16 September 2010.

[15] Zhu, Z. Q., Al-Ani, M. M. J., Liu, X., *et al.*: 'Comparative study of torque-speed characteristics of alternate switched-flux permanent magnet machine topologies', Proc. PEMD 2012, Bristol, UK, 27-29 March 2012.

[16] Zhao, G., Tian, L., Shen, Q., *et al.*: 'Demagnetization analysis of permanent magnet synchronous machines under short circuit fault', Proc. APPEEC 2010, Chengdu, 28-31 March 2010.

[17] Ruoho, S., Kolehmainen, J., Ikäheimo, J., *et al.*: 'Interdependence of demagnetization, loading, and temperature rise in a permanent-magnet synchronous motor', IEEE Trans. Magn., **46**, (3), March 2010, pp. 949-953.

[18] Zhou, P., Lin, D., Xiao, Y., *et al.*: 'Temperature-dependent demagnetization model of permanent magnets for finite element analysis', IEEE Trans. Magn., **48**, (2), February 2012, pp. 1031-1034.

[19] McFarland, J. D., Jahns, T. M., EL-Refaie, A. M.: 'Demagnetization performance characteristics of flux switching permanent magnet machines', Proc. ICEM2014, Berlin, 2-5 September 2014.

[20] Li, S., Li, Y., Sarlioglu, B.: 'Partial irreversible demagnetization assessment of flux switching permanent magnet machine using ferrite permanent magnet material', IEEE Trans. Magn., **51**, (7), July 2015, pp. 1-9.

[21] Zhu, S., Cheng, M., Hua, W., *et al.*: 'Finite element analysis of flux-switching PM machine considering oversaturation and irreversible demagnetization', IEEE Trans. Magn., **51**, (11), November 2015, pp. 1-4.

[22] Afinowi, I. A. A., Zhu, Z. Q., Guan, Y., *et al.*: 'Performance analysis of switched-flux machines with hybrid NdFeB and ferrite magnets', in Proc. of ICEMS 2014, Hangzhou, 22-25 October 2014.

[23] Bellini, A., Filippetti, F., Tassoni, C. *et al.*: 'Advances in Diagnostic Techniques for Induction Machines', IEEE Trans. Ind. Electron., **55**, (12), December 2008, pp. 4109-4126.

[24] ‘Arnold Magnetic Technologies’, http://www.arnoldmagnetics.com/uploadedFiles/Library/pdf/, accessed 10 July 2015.

[25] Ruoho, S., Dlala, E., Arkkio, A.: ‘Comparison of demagnetization models for finite-element analysis of permanent-magnet synchronous machines’, IEEE Trans. Magn., **43**, (11), November 2007, pp. 3964 - 3968.

[26] Kaiser, K. L.: ‘Electromagnetic Compatibility Handbook’ (CRC Press, 2004).

[27] Campbell, P.: ‘Permanent Magnet Materials and their Application’ (Cambridge University Press, 1996, pp. 93-96).

[28] Li, G. J.: ‘Contribution à la conception des machines electriques à rotor passif pour des applications critiques: modélisations electromagnétiques et thermiques sur cycle de fonctionnement, etude du fonctionnement en mode dégradé’, PhD Thesis, July 2011.

[29] Vaseghi, B., Nahid-Mobarakh, B., Takorabet, N., *et al.*: ‘Inductance Identification and Study of PM Motor with Winding Turn Short Circuit Fault’, IEEE Trans. Magn., **47**, (5), May 2011, pp. 978-981.

[30] Ben Sedrine, E., Ojeda, J., Gabsi, M., *et al.*:, ‘Fault-tolerant control using the GA optimization considering the reluctance torque of a five-phase flux switching machine’, IEEE Trans. Energy Convers., **30**, (3), September 2015, pp. 927-938.

[31] Chu, W. Q., Zhu, Z. Q.: ‘Average torque separation in permanent magnet synchronous machines using frozen permeability’, IEEE Trans. Magn., **49**, (3), March 2013, pp. 1202-1210.